

Synthetically enhanced sensitivity using higher-order exceptional point and coherent perfect absorption

Yao-Dong Hu,¹ Yi-Pu Wang,^{1*} Rui-Chang Shen,¹ Zi-Qi Wang,¹
Wei-Jiang Wu,¹ J. Q. You^{1,2†}

¹ Zhejiang Province Key Laboratory of Quantum Technology and Device, School of Physics, and State Key Laboratory for Extreme Photonics and Instrumentation, Zhejiang University, Hangzhou 310027, China

² College of Optical Science and Engineering, Zhejiang University, Hangzhou 310027, China

E-mail: yipuwang@zju.edu.cn and jqyou@zju.edu.cn

November 2023

Abstract. Sensors play a crucial role in advanced apparatuses and it is persistently pursued to improve their sensitivities. Recently, the singularity of a non-Hermitian system, known as the exceptional point (EP), has drawn much attention for this goal. Response of the eigenfrequency shift to a perturbation ϵ follows the $\epsilon^{1/n}$ -dependence at an n th-order EP, leading to significantly enhanced sensitivity via a high-order EP. However, due to the requirement of increasingly complicated systems, great difficulties will occur along the path of increasing the EP order to enhance the sensitivity. Here we report that by utilizing the spectral anomaly of the coherent perfect absorption (CPA), the sensitivity at a third-order EP can be further enhanced owing to the cooperative effects of both CPA and EP. We realize this synthetically enhanced sensor using a pseudo-Hermitian cavity magnonic system composed of two yttrium iron garnet spheres and a microwave cavity. The detectable minimum change of the magnetic field reaches 4.2×10^{-21} T. It opens a new avenue to design novel sensors using hybrid non-Hermitian quantum systems.

1. Introduction

Non-Hermitian systems are ubiquitous in nature, owing to the flow of energy, particles, and information to and from the external degrees of freedom that lie outside the Hilbert space of the considered system [1]. They exhibit characteristics distinct from the Hermitian counterparts [2, 3, 4, 5]. A critical advancement of the non-Hermitian physics is related to the singularity of the system, known as the exceptional point (EP) [6, 7], where eigenvalues become degenerate and the corresponding eigenvectors coalesce. This singularity brings new possibilities for intriguing applications, including the optical isolation [8, 9, 10], band merging [11, 12], loss-induced transparency [13],

asymmetric mode switching [14], single-mode lasers [15, 16, 17, 18], and topological chirality [19, 20, 21, 22, 23]. Novel properties at or around the EP have been achieved in a vast array of platforms, such as microwave [19, 10], photonic [11, 12, 13, 14, 15, 16, 20, 21, 24, 25, 26], magnetic [27, 28], acoustic [29], mechanical [22], and optomechanical systems [30, 31].

Recently, EP-based sensors have attracted considerable interest due to the enhanced response to the external perturbation, providing an efficient way to boost detection sensitivity [32, 33, 34, 35, 36, 37, 38, 39]. The eigenfrequency splitting at the n th-order EP (i.e., EP n) follows a $\epsilon^{1/n}$ -dependence (where ϵ denotes the perturbation amplitude), which indicates that a higher-order EP is beneficial to higher sensitivity. Indeed, successful demonstrations of the enhanced sensitivity have been realized at the EP3 [33, 34], but great difficulties will occur along the path of further increasing the EP order to enhance the sensitivity. This is because the achievement of higher-order EPs requires more precise parameter controls. Thus, to further increase the sensitivity of EP-based sensors, it is necessary to contemplate new mechanisms. In this work, we achieve the EP3 of a pseudo-Hermitian Hamiltonian [40, 41], which is implemented using a cavity magnonic system via precisely adjusting multi-parameters [27, 42]. The coherent perfect absorption (CPA) [43, 44, 45, 46, 47, 48] is also used to further enhance the sensitivity at the EP3. The resulting sensitivity is remarkably enhanced owing to the *cooperative* effects of both CPA and EP3. A formulated explanation of this synthetic sensitivity can be characterized by the detectable minimum change of the magnetic field,

$$\delta B_{\min} = 2\pi \frac{\delta A}{\gamma_e G_{\text{CPA}} G_{\text{EP3}}}, \quad (1)$$

where γ_e is the gyromagnetic ratio of the ferrimagnetic material that we use ($\gamma_e = 2\pi * 28$ GHz/T), and δA represents the smallest spectrum change that can be resolved in the experiment (e.g., 1×10^{-13} dB). G_{CPA} and G_{EP3} are sensitivity factors associated with the CPA and EP3, respectively. It is clear that the sensitivity induced by these two mechanisms is superimposed in a *product* form, thus yielding a vast enhancement. Our work paves a novel way to greatly enhance the sensitivity using both CPA and EP in a single non-Hermitian system.

2. Pseudo-Hermitian cavity magnonic system

2.1. Experimental setup

The cavity magnonic system consists of a three-dimensional (3D) rectangular cavity ($50 \times 25 \times 7.5$ mm³) and two 0.5 mm-diameter yttrium iron garnet (YIG) spheres [figure 1(a)]. The two ports of the cavity are connected to a vector network analyzer (VNA) for both loading microwave signals and implementing measurement. The power ratio and phase difference of the two signals are controlled by a variable attenuator (VA) and a variable phase shifter (VPS), respectively. Here, the CPA is realized by precisely adjusting the VA and VPS to achieve zero output signals from the cavity.

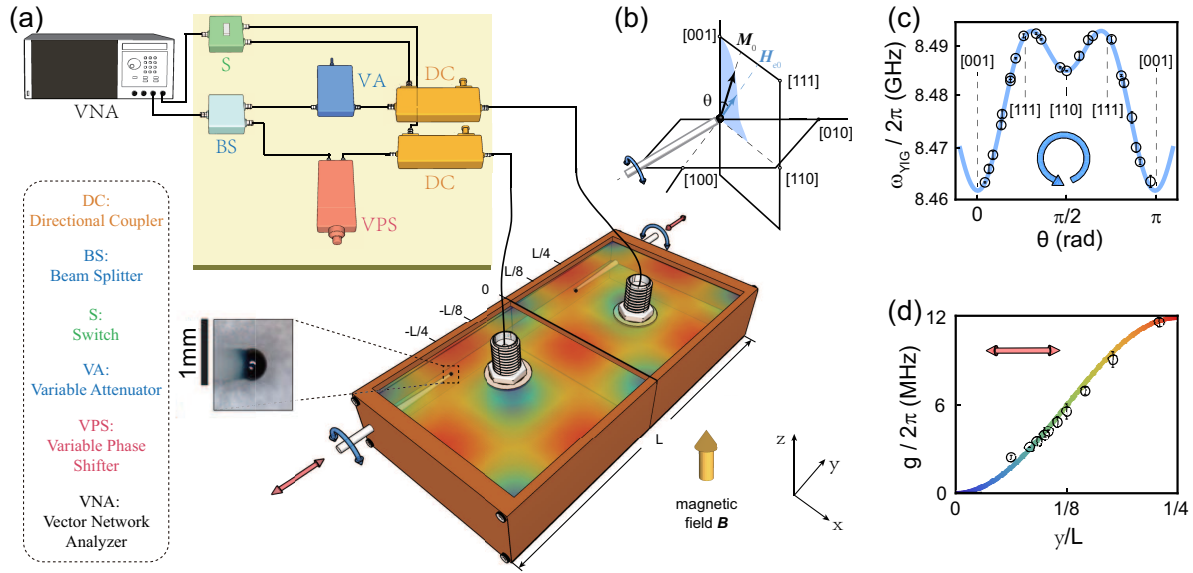


Figure 1. Schematic diagrams of the experimental setup and parameter adjustments. (a) The microwave signal generated by a vector network analyzer (VNA) is divided into two signals by a beam splitter (BS). These two signals are subsequently tuned by a variable attenuator (VA) and a variable phase shifter (VPS), respectively, to match the CPA condition. Then, the signals are loaded into the cavity via two directional couplers (DC), by which the output signals are sent back to the VNA. Two 0.5 mm-diameter YIG spheres are placed in the cavity. The magnetic-field distribution of the cavity mode TE_{102} is shown as a colour diagram. (b) The magnetocrystalline anisotropy field is employed to tune the frequency of the magnon mode. (c) The frequency of the magnon mode (circles) is measured by rotating the YIG sphere. (d) The coupling strength between the magnon mode and the cavity mode (circles) is tuned by moving the YIG sphere from 0 to $L/4$, where L is the length of the cavity. The curves in (c) and (d) are theoretical results.

The dissipation rates of the cavity ports are tuned by changing the lengths of antenna pins inserted into the cavity (Appendix A). Each YIG sphere is glued on a plastic rod to adjust its position and crystal axis orientation. After applying a bias magnetic field \mathbf{B} in the z -direction, magnon modes are supported in the sphere. Here we focus on the Kittel mode, i.e., the uniform precession mode of the spin ensemble. By moving the YIG sphere along the edge of the cavity (y -direction), the coupling strength between the magnon and cavity modes can be precisely controlled. Meanwhile, rotating the rod can change the frequency of the magnon mode owing to the magnetocrystalline anisotropy [42]. Specifically, rotating the rod from 0° to 180° changes the magnon frequency in a range of 0.3 GHz [figures 1(b) and 1(c)]. When the position of the YIG sphere is tuned from 0 to $\pm L/4$, the coupling strength between the magnon and cavity modes can be tuned from 0 to 12 MHz [figure 1(d)]. With these control parameters, we can simultaneously realize the CPA and EP3 in the system.

2.2. Pseudo-Hermitian system with a third-order exceptional point

The non-Hermitian Hamiltonian of the system with CPA can be written, in the rotating frame associated with the cavity frequency (details in Appendix B):

$$H/\hbar = \begin{pmatrix} i\kappa_c & g_1 & g_2 \\ g_1 & \Delta_1 - i\gamma_1 & 0 \\ g_2 & 0 & \Delta_2 - i\gamma_2 \end{pmatrix}, \quad (2)$$

where $\kappa_c \equiv \kappa_1 + \kappa_2 - \kappa_{\text{int}} > 0$ is the effective gain of the cavity mode, g_1 (g_2) is the coupling strength between the cavity mode and the magnon mode in the YIG sphere 1 (2), which has decay rate γ_1 (γ_2), and Δ_1 (Δ_2) = ω_1 (ω_2) - ω_c is the frequency detuning between the cavity mode and the corresponding magnon mode.

In the symmetric case, we have two identical YIG spheres ($\gamma_1 = \gamma_2 = \gamma$) and the same coupling strengths $g_1 = g_2 = g$. Also, the effective gain of the cavity is tuned to $\kappa_c = 2\gamma$, and $\Delta_1 = -\Delta_2 \equiv \Delta$. Then, the Hamiltonian reduces to

$$H/\hbar = \begin{pmatrix} 2i\gamma & g & g \\ g & \Delta - i\gamma & 0 \\ g & 0 & -\Delta - i\gamma \end{pmatrix}. \quad (3)$$

The eigenvalues of this Hamiltonian are determined by $\text{Det}(H - \Omega I) = 0$, which gives the characteristic polynomial,

$$\Omega^3 + c_1\Omega + c_0 = 0, \quad (4)$$

with $c_0 = 2i\gamma(\Delta^2 + \gamma^2 - g^2)$, and $c_1 = 3\gamma^2 - 2g^2 - \Delta^2$. Here $\Omega \equiv \omega - \omega_c$ is the biased eigenvalue of the system and I is the identity matrix. According to the Cardano formula, the eigenvalues of the system can be explicitly written as

$$\begin{aligned} \Omega^{(0)} &= \sqrt[3]{\frac{c_0}{2} + \sqrt{\frac{c_0^2}{4} + \frac{c_1^3}{27}}} + \sqrt[3]{\frac{c_0}{2} - \sqrt{\frac{c_0^2}{4} + \frac{c_1^3}{27}}}, \\ \Omega^{(1)} &= \sqrt[3]{\frac{c_0}{2} + \sqrt{\frac{c_0^2}{4} + \frac{c_1^3}{27}}} \left(-\frac{1}{2} + i\frac{\sqrt{3}}{2}\right) - \sqrt[3]{\frac{c_0}{2} - \sqrt{\frac{c_0^2}{4} + \frac{c_1^3}{27}}} \left(-\frac{1}{2} + i\frac{\sqrt{3}}{2}\right)^2, \\ \Omega^{(2)} &= \sqrt[3]{\frac{c_0}{2} + \sqrt{\frac{c_0^2}{4} + \frac{c_1^3}{27}}} \left(-\frac{1}{2} + i\frac{\sqrt{3}}{2}\right)^2 - \sqrt[3]{\frac{c_0}{2} - \sqrt{\frac{c_0^2}{4} + \frac{c_1^3}{27}}} \left(-\frac{1}{2} + i\frac{\sqrt{3}}{2}\right). \end{aligned} \quad (5)$$

In figures 2(a) and 2(b), we plot these three eigenvalues versus both g and Δ .

(i) When $g = \sqrt{\Delta^2 + \gamma^2}$, i.e., $c_0 = 0$, the three eigenvalues in equation (5) are reduced to

$$\Omega^{(0)} = 0, \quad \Omega^{(\pm)} = \pm\sqrt{3g^2 - 4\gamma^2}, \quad (6)$$

which are drawn as the red curves in figures 2(a) and 2(b). Note that the non-Hermitian Hamiltonian (3) with $g = \sqrt{\Delta^2 + \gamma^2}$ does not have the parity-time (PT) symmetry, but

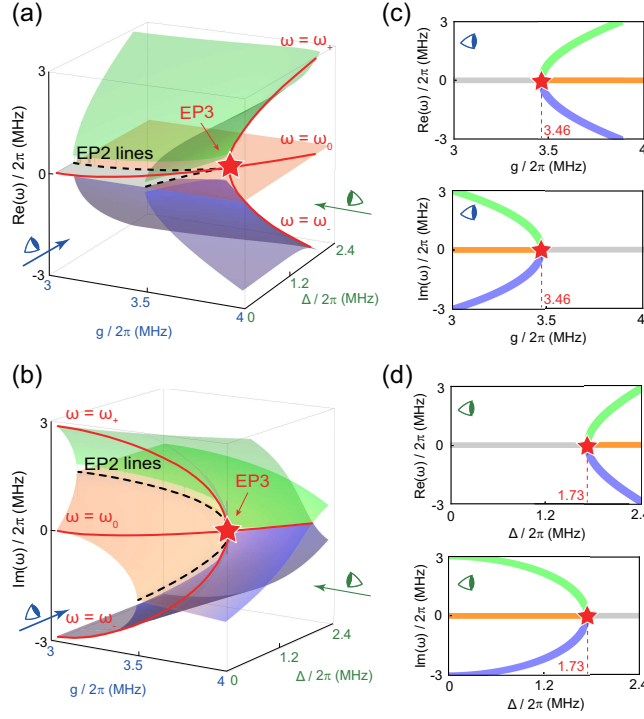


Figure 2. Eigenvalues of the three-mode non-Hermitian system. (a) and (b) Real and imaginary parts of the three eigenvalues versus the coupling strength $g/2\pi$ and frequency detuning $\Delta/2\pi$, as illustrated by the green, orange and purple surfaces, respectively. The EP2 lines are indicated as the black dashed curves, and the intersection point of the two curves is the EP3 (red star). (c) Real and imaginary parts of the eigenvalues versus $g/2\pi$, corresponding to the side views of (a) and (b) by the “blue” eye. The value of $g/2\pi$ at EP3 is $g_{EP3}/2\pi = 3.46$ MHz. (d) Real and imaginary parts of the eigenvalues versus $\Delta/2\pi$, corresponding to the side views of (a) and (b) by the “green” eye. The value of $\Delta/2\pi$ at EP3 is $\Delta_{EP3}/2\pi = 1.73$ MHz. (c) and (d) give the three eigenvalues of the pseudo-Hermitian Hamiltonian.

can still have three real eigenvalues when $g > g_{EP3} \equiv 2\gamma/\sqrt{3}$. This is because the non-Hermitian Hamiltonian becomes *pseudo-Hermitian* in this case [40, 41, 49, 50]. When $g < g_{EP3}$, $\Omega^{(\pm)}$ become complex, i.e., one of the three eigenvalues is real ($\Omega^{(0)} = 0$) and the other two, $\Omega^{(\pm)}$, are a complex-conjugate pair. In particular, when $g = g_{EP3} \equiv 2\gamma/\sqrt{3}$, there is $\Delta = \Delta_{EP3} \equiv \gamma/\sqrt{3}$ owing to the relation $g = \sqrt{\Delta^2 + \gamma^2}$. Now, the three eigenvalues coalesce to $\Omega^{(\pm)} = \Omega^{(0)} = 0$. In figures 2(c) and 2(d), these three eigenvalues of the pseudo-Hermitian Hamiltonian are shown versus g and Δ , respectively.

Corresponding to the three eigenvalues in equation (6), the pseudo-Hermitian Hamiltonian, i.e., the non-Hermitian Hamiltonian (3) with $g = \sqrt{\Delta^2 + \gamma^2}$,

have the following eigenvectors:

$$\begin{aligned}
 |\Phi_0\rangle &= \begin{pmatrix} 1 \\ \frac{-\sqrt{g^2-\gamma^2-i\gamma}}{g} \\ \frac{\sqrt{g^2-\gamma^2-i\gamma}}{g} \end{pmatrix}, \\
 |\Phi_+\rangle &= \begin{pmatrix} 1 \\ \frac{g}{\sqrt{3g^2-4\gamma^2-\sqrt{g^2-\gamma^2+i\gamma}}} \\ \frac{g}{\sqrt{3g^2-4\gamma^2+\sqrt{g^2-\gamma^2+i\gamma}}} \end{pmatrix}, \\
 |\Phi_-\rangle &= \begin{pmatrix} 1 \\ \frac{g}{-\sqrt{3g^2-4\gamma^2-\sqrt{g^2-\gamma^2+i\gamma}}} \\ \frac{g}{-\sqrt{3g^2-4\gamma^2+\sqrt{g^2-\gamma^2+i\gamma}}} \end{pmatrix}.
 \end{aligned} \tag{7}$$

At $g = g_{\text{EP3}} \equiv 2\gamma/\sqrt{3}$, these three eigenvectors coalesce to

$$|\Phi_{\pm}\rangle = |\Phi_0\rangle = \begin{pmatrix} 1 \\ \frac{-1-i\sqrt{3}}{2} \\ \frac{1-i\sqrt{3}}{2} \end{pmatrix}, \tag{8}$$

revealing that $g_{\text{EP3}} \equiv 2\gamma/\sqrt{3}$ is indeed the third-order exceptional point (EP3) of the pseudo-Hermitian Hamiltonian.

(ii) The three eigenvalues in equation (5) have EP2 lines when $27c_0^2 + 4c_1^3 = 0$. In this case, the three eigenvalues reduce to

$$\begin{aligned}
 \Omega^{(0)} &= 2\sqrt[3]{\frac{c_0}{2}}, \\
 \Omega^{(1)} &= i\sqrt{3}\sqrt[3]{\frac{c_0}{2}}, \\
 \Omega^{(2)} &= -i\sqrt{3}\sqrt[3]{\frac{c_0}{2}},
 \end{aligned} \tag{9}$$

Furthermore, when $c_0 = 0$, it follows from $27c_0^2 + 4c_1^3 = 0$ that $c_1 = 0$ as well, which corresponds to the critical parameters $g = g_{\text{EP3}} \equiv 2\gamma/\sqrt{3}$, and $\Delta = \Delta_{\text{EP3}} \equiv \gamma/\sqrt{3}$. Now, the three eigenvalues in equation (9) coalesce to $\Omega^{(0)} = \Omega^{(1)} = \Omega^{(2)} = 0$. This corresponds to the case where the EP2 lines intersect at the EP3, as shown in figures 2(a) and 2(b).

3. Results and discussions

3.1. Output spectra at and away from EP3

In the experiment, we utilize a small variation of the external magnetic field as the perturbation, which results in a frequency change Δ_B for the Kittel mode of each YIG

sphere. The perturbed pseudo-Hermitian Hamiltonian has been shown in equation (10), where the system has the eigenvalue shift $\Delta_\omega \equiv \Omega' - \Omega$ under the perturbation Δ_B . In figures 3(a) and 3(b), we measure the output spectra to demonstrate the response of the pseudo-Hermitian system to Δ_B *at* and *away from* the EP3. The darkest red areas correspond to the system with (or nearly with) CPA under zero (or small) perturbation Δ_B . It is clear that each of the three eigenvalue has a frequency shift in the case of $g > g_{\text{EP3}}$ when applying the perturbation Δ_B [figure 3(b)], while these frequency shifts become the same at the EP3 ($g = g_{\text{EP3}}$) because all eigenvalues coalesce there [figure 3(a)]. Hereafter, we focus on the central eigenvalue $\Omega = 0$ of the pseudo-Hermitian Hamiltonian, so $\Omega' = \Delta_\omega$.

3.2. Perturbation-induced eigenfrequency shift

The perturbation of the external magnetic field can induce frequency change of the Kittel mode in each YIG sphere. In our experiment, we use two identical YIG spheres, so these frequency changes can be nearly identical. By considering the magnetic-field perturbation, the pseudo-Hermitian Hamiltonian, i.e., the Hamiltonian (3) with $\Delta = \sqrt{g^2 - \gamma^2}$, can be converted to

$$H'/\hbar = \begin{pmatrix} 2i\gamma & g & g \\ g & \sqrt{g^2 - \gamma^2} + \Delta_B - i\gamma & 0 \\ g & 0 & -\sqrt{g^2 - \gamma^2} + \Delta_B - i\gamma \end{pmatrix}, \quad (10)$$

where Δ_B is the frequency change of the Kittel mode induced by the magnetic-field perturbation. From the eigenvalue equation $\text{Det}(H' - \Omega'I) = 0$, we can obtain the relation between the eigenvalue $\Omega'(\Delta_B) \equiv \omega'(\Delta_B) - \omega_c$ and the frequency change Δ_B , which is

$$\frac{2\Delta_B - \Omega'}{g^2} + \frac{4(g^2 - \gamma^2)(\Omega' - \Delta_B)}{[(\Omega' - \Delta_B)^2 + g^2]^2 - 4(g^2 - \gamma^2)(\Omega' - \Delta_B)^2} = 0, \quad (11)$$

where $\Omega'(\Delta_B) \equiv \omega'(\Delta_B) - \omega_c$ reduces to the eigenvalue $\Omega \equiv \omega - \omega_c$ of the pseudo-Hermitian Hamiltonian when $\Delta_B = 0$.

For a sufficiently small perturbation Δ_B , we can ignore the higher-order terms $O(\Delta_B^2)$ and write the relation between Δ_B and Ω' as

$$\Delta_B = \frac{\Omega^3(\Omega'^2 + g^2) - (3g^2 - 4\gamma^2)(\Omega'^2 + g^2)\Omega'}{g^4 + 2\Omega'^2(\Omega'^2 + 2g^2) - (3g^2 - 4\gamma^2)(4\Omega'^2 + g^2)}. \quad (12)$$

Based on equation (12), we can study the response of the eigenfrequency to the perturbation.

We define the perturbation-induced eigenfrequency shift as

$$\Delta_\omega \equiv \omega'(\Delta_B) - \omega = \Omega'(\Delta_B) - \Omega. \quad (13)$$

Here we focus on the *central* branch of the eigenvalues of the pseudo-Hermitian Hamiltonian, i.e., $\Omega = \Omega^{(0)} = 0$ [cf. equation (6)].

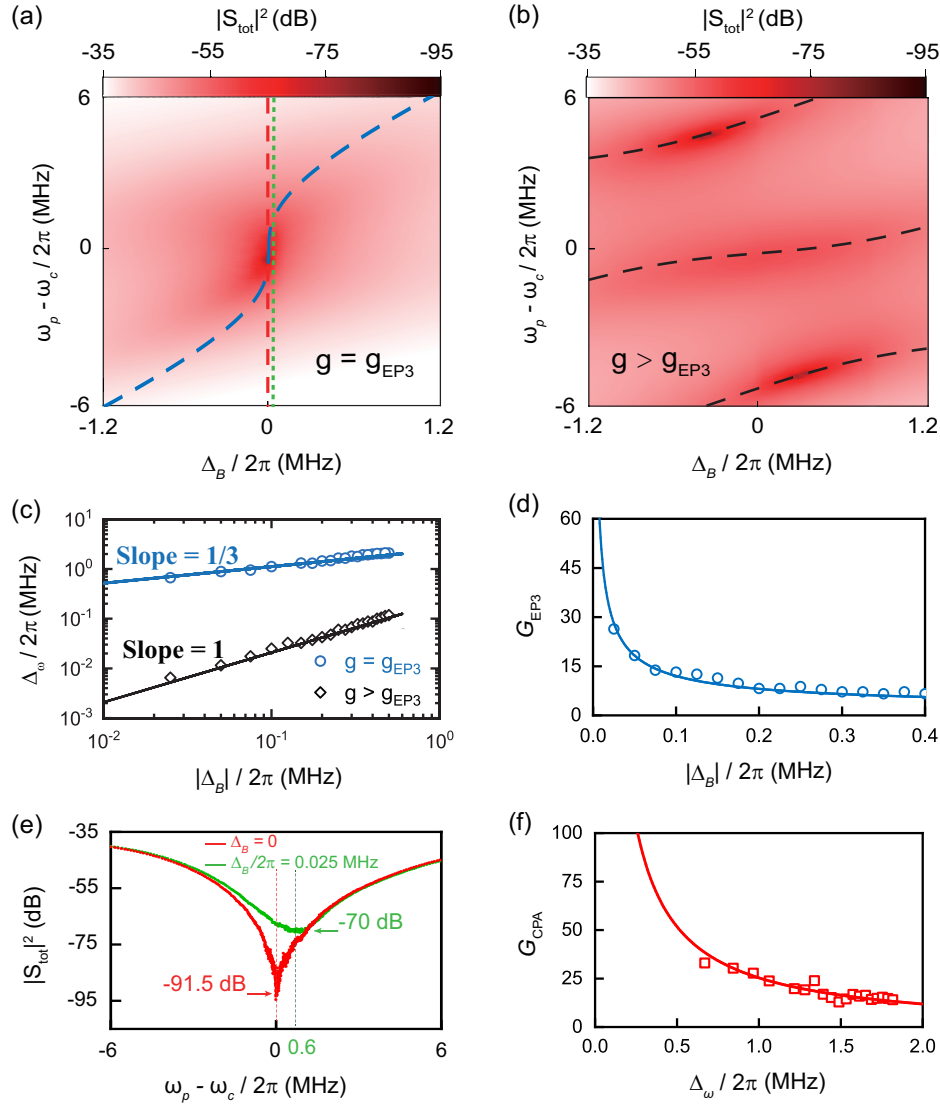


Figure 3. Output spectra and sensitivity factors. (a) Total output spectrum at the EP3 ($g = g_{\text{EP3}} = 2\pi \times 3.46$ MHz) versus the perturbation $\Delta_B/2\pi$, where the dashed and dotted vertical lines correspond to $\Delta_B/2\pi = 0$ and 0.025 MHz, respectively. (b) Total output spectrum away from the EP3 ($g = 2\pi \times 4.59$ MHz $> g_{\text{EP3}}$) versus the perturbation $\Delta_B/2\pi$. Dashed curves in (a) and (b) are eigenfrequency shifts $\Delta_\omega = \Omega' - \Omega$ obtained by diagonalizing the Hamiltonian, i.e. equation (10). (c) Log-log plot of the frequency shift $\Delta_\omega/2\pi$ of the central eigenvalue versus $|\Delta_B|/2\pi$ at $g/2\pi = 3.46$ and 4.59 MHz, respectively. The slopes 1/3 and 1 are fitted using equations (16) and (19), respectively. (d) Sensitivity factor at the EP3 versus $|\Delta_B|/2\pi$. (e) Total output spectra extracted at $\Delta_B/2\pi = 0$ and 0.025 MHz, corresponding to the two vertical lines in (a). The spectral dip at $\Delta_B = 0$ has the minimum value -91.5 dB. (f) CPA-related sensitivity factor G_{CPA} versus the eigenfrequency shift $\Delta_\omega/2\pi$.

(i) At the EP3, i.e., $g = g_{\text{EP3}} \equiv 2\gamma/\sqrt{3}$, equation (12) reduces to

$$\Delta_B = \frac{\Omega'^3 (\Omega'^2 + g_{\text{EP3}}^2)}{g_{\text{EP3}}^4 + 2\Omega'^2 (\Omega'^2 + 2g_{\text{EP3}}^2)}. \quad (14)$$

For a small perturbation, we can assume that Ω' is close to $\Omega = \Omega^{(0)} = 0$ such that $\Omega' \ll g$. Then, it follows from equation (14) that

$$\Delta_B = \frac{\Omega'^3}{g_{\text{EP3}}^2} = \frac{\Delta_\omega^3}{g_{\text{EP3}}^2}, \quad (15)$$

i.e.,

$$\Delta_\omega = g_{\text{EP3}}^{2/3} \Delta_B^{1/3}, \quad (16)$$

where the $\Delta_B^{1/3}$ dependence is characteristic of the EP3.

From equation (16), we obtain the sensitivity factor at the EP3:

$$G_{\text{EP3}} \equiv \left(\frac{\Delta_\omega}{\Delta_B} \right)_{\text{EP3}} = \frac{g_{\text{EP3}}^{2/3}}{\Delta_B^{2/3}}. \quad (17)$$

It tends to infinity when $\Delta_B \rightarrow 0$, indicating the singular behavior at the EP3. In figure 3(d), we numerically show the relation between the sensitivity factor G_{EP3} and the perturbation Δ_B .

(ii) Away from the EP3, there is $g \neq g_{\text{EP3}} \equiv 2\gamma/\sqrt{3}$. For a small perturbation, we can still assume that $\Omega' \ll g$ and then equation (12) is reduced to

$$\Delta_B = -\frac{(3g^2 - 4\gamma^2) \Omega'}{g^2 - (3g^2 - 4\gamma^2)}, \quad (18)$$

which gives a *linear* dependence of the eigenfrequency shift on the perturbation Δ_B ,

$$\Delta_\omega = \left(1 - \frac{g^2}{3g^2 - 4\gamma^2} \right) \Delta_B. \quad (19)$$

Figure 3(c) shows the frequency shift Δ_ω of the central eigenvalue versus $|\Delta_B|$. Theoretically, at the EP3, this eigenfrequency shift is $\Delta_\omega = g^{2/3} \Delta_B^{1/3}$, while $\Delta_\omega \sim \Delta_B$ away from the EP3. These theoretical results fit well with the experimental data. The sensitivity factor at the EP3 [figure 3(d)] can be defined by

$$G_{\text{EP3}} \equiv \left(\frac{\Delta_\omega}{\Delta_B} \right)_{\text{EP3}} = g^{2/3} \Delta_B^{-2/3}. \quad (20)$$

Compared with the case away from the EP3, the eigenvalue shift Δ_ω shows a *steep* slope at the EP3, yielding a more profound amplification of the eigenfrequency shift under the same perturbation Δ_B .

3.3. Enhanced sensing using CPA

In our experiment, the parameters of the system are chosen to achieve the pseudo-Hermitian Hamiltonian, i.e., the Hamiltonian (3) with $g = \sqrt{\Delta^2 + \gamma^2}$, but the CPA condition is not obeyed in some cases for comparison. With these parameters, it follows from equation (C.8) in Appendix C that the total output spectrum is given by

$$|S_{\text{tot}}(\Omega)|^2 = \frac{(p+1) \left| [m(\Omega) + 2\sqrt{\kappa_1\kappa_2}e^{i\phi}/\sqrt{p} + 2\kappa_1] + in(\Omega) \right|^2}{m(\Omega)^2 + n(\Omega)^2} + \frac{\left(\sqrt{p}e^{-i\phi} - \sqrt{\kappa_1/\kappa_2} \right) k(\Omega)}{m(\Omega)^2 + n(\Omega)^2}, \quad (21)$$

with

$$k(\Omega) = 4 \left(\sqrt{\kappa_1\kappa_2} + \kappa_2 e^{i\phi}/\sqrt{p} \right)^2 \left(\sqrt{p}e^{-i\phi} - \sqrt{\kappa_1/\kappa_2} \right) + 4 \left(\sqrt{\kappa_1\kappa_2} + \kappa_2 e^{i\phi}/\sqrt{p} \right) [m(\Omega) + 2\sqrt{\kappa_1\kappa_2}e^{i\phi}/\sqrt{p} + 2\kappa_1], \quad (22)$$

$$m(\Omega) = 2\gamma - 2\kappa_1 - 2\kappa_2 - \frac{g^2\gamma}{(\Omega - \Delta)^2 + \gamma^2} - \frac{g^2\gamma}{(\Omega + \Delta)^2 + \gamma^2}, \quad (23)$$

$$n(\Omega) = \Omega - \frac{g^2(\Omega - \Delta)}{(\Omega - \Delta)^2 + \gamma^2} - \frac{g^2(\Omega + \Delta)}{(\Omega + \Delta)^2 + \gamma^2}, \quad (24)$$

where $g = \sqrt{\Delta^2 + \gamma^2}$, and $\Omega = \omega - \omega_c$, while p and ϕ denote the power ratio and phase difference between the two input field, respectively. When the perturbation is applied, the output spectrum $|S'_{\text{tot}}(\Omega')|^2$ has the same form as equation (21), but Ω is replaced by $\Omega' = \omega' - \omega_c$ and $\pm\Delta$ in equation. (22) are replaced by $\Delta + \Delta_B$ and $-\Delta + \Delta_B$, respectively.

In the presence of CPA, it follows from equation (B.4) that $\sqrt{p}e^{-i\phi} = \sqrt{\kappa_1/\kappa_2}$. The output spectrum in equation (21) is reduced to

$$|S_{\text{tot}}(\Omega)|_{\text{CPA}}^2 = (\kappa_1/\kappa_2 + 1) \frac{\Omega^2 (\Omega^2 - 3g^2 + 4\gamma^2)^2}{(\Omega^2 - g^2)^2 + 4\Omega^2\gamma^2} / [m(\Omega)^2 + n(\Omega)^2]. \quad (25)$$

Here $|S_{\text{tot}}(\Omega)|_{\text{CPA}}^2$ reaches its minimum value 0 when $\Omega = 0$ or $\Omega = \pm\sqrt{3g^2 - 4\gamma^2}$, which are exactly the eigenvalues of the pseudo-Hermitian Hamiltonian given in equation (6).

Without the perturbation Δ_B , our system has been tuned to exhibit the CPA, and it can exhibit nearly CPA under a small Δ_B . In decibels, the output spectrum of the system with CPA has an extremely sharp dip, but a less sharp dip occurs in the system nearly with CPA [cf. figure 3(e)]. In the present experiment, we focus on the central branch of the three eigenvalues, i.e., $\Omega = \Omega^{(0)} = 0$. We can define a sensitivity factor related to the CPA:

$$G_{\text{CPA}} \equiv 2\pi \frac{\Delta |S_{\text{tot}}^{(\min)}|^2}{\Delta_\omega} = \frac{10 \log_{10} |S'_{\text{tot}}^{(\min)}(\Delta_\omega)|^2 - 10 \log_{10} |S_{\text{tot}}^{(\min)}(0)|_{\text{CPA}}^2}{(\Delta_\omega/2\pi)}, \quad (26)$$

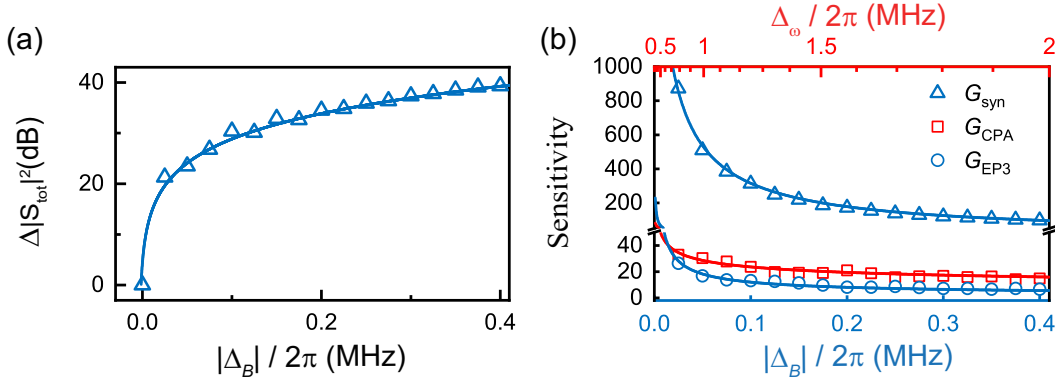


Figure 4. Synthetically enhanced sensitivity in the presence of both CPA and EP3. (a) Minimum-value changes of the output spectra $\Delta|S_{\text{tot}}^{(\min)}|^2$ at the EP3 versus the perturbation $\Delta_B/2\pi$. (b) Synthetic sensitivity factor G_{syn} in comparison with the respective sensitivity factors G_{CPA} and G_{EP3} . Curves are the corresponding fitting results.

where $|S_{\text{tot}}^{(\min)}(0)|_{\text{CPA}}^2$ is the minimum value of the output spectrum in the presence of CPA, where $\Omega = 0$, and $|S_{\text{tot}}^{\prime(\min)}(\Delta_\omega)|^2$ is the minimum value of the corresponding output spectrum under the perturbation Δ_B , where $\Omega' = \Delta_\omega$. Because $|S_{\text{tot}}^{\prime(\min)}(\Delta_\omega)|^2 \neq 0$ and $|S_{\text{tot}}^{(\min)}(0)|_{\text{CPA}}^2 = 0$, $10 \log_{10} |S_{\text{tot}}^{(\min)}(0)|_{\text{CPA}}^2 \rightarrow -\infty$, giving rise to $G_{\text{CPA}} \rightarrow \infty$ in the ideal case. However, in a practical experiment, $10 \log_{10} |S_{\text{tot}}^{(\min)}(0)|_{\text{CPA}}^2$ cannot reach $-\infty$, but it can reach -91.5 dB here at the EP3, resulting from the limited measurement precision of the VNA and the limited adjusting accuracy of the system parameters. Nevertheless, this minimum value can still produce a significantly large enhancement factor G_{CPA} at the EP3 [cf. figure 3(f)], especially in the case of small Δ_ω .

3.4. Synthetic sensitivity in the presence of both CPA and EP3

Based on the experimental data of the output spectra, we obtain the observed changes of the minimum values of the output spectra $\Delta|S_{\text{tot}}^{(\min)}|^2$ at the EP3 versus the perturbation Δ_B , as shown in figure 4(a). From this relationship between $\Delta|S_{\text{tot}}^{(\min)}|^2$ and Δ_B , we can define the synthetically enhanced sensitivity of the system in the presence of both CPA and EP3, $G_{\text{syn}} \equiv 2\pi\Delta|S_{\text{tot}}^{(\min)}|^2/\Delta_B$, which is readily given by $G_{\text{syn}} = G_{\text{CPA}}G_{\text{EP3}}$. Figure 4(b) shows the obtained G_{syn} versus the perturbation Δ_B , in comparison with the corresponding G_{CPA} and G_{EP3} . Because the enhancements related to the CPA and EP3 are combined in a *product* form, the synthetic enhancement factor becomes significantly greater than the respective enhancement factors [figure 4(b)]. This clearly demonstrates the distinct advantage of using both CPA and EP3 in a single non-Hermitian system to produce a sensor with high sensitivity.

3.5. Detectable minimum change of the magnetic field

Finally, we discuss the limit of the minimum magnetic-field change that can be detected by the current synthetically enhanced sensor. For the YIG sphere, the relation between the applied magnetic field and the frequency of the uniform magnon mode is

$$\omega_m = \gamma_e |\vec{B}| + \omega_{m,0}, \quad (27)$$

where $\gamma_e/2\pi = 28$ GHz/T denotes the gyromagnetic ratio and $\omega_{m,0}$ is determined by the anisotropy field. In the synthetically enhanced sensor, the adjustment of the magnetic field is limited by the smallest change of the current supply, i.e., 1×10^{-4} A, in our electromagnet. The measured frequency change of the magnon mode is $\Delta_B/2\pi = (\omega'_m - \omega_m)/2\pi \approx 0.025$ MHz, where ω'_m (ω_m) is the frequency of the magnon mode with (without) the perturbation. It follows from $\Delta_B = \gamma_e \delta B$ that the corresponding magnetic-field change is $\delta B \approx 9 \times 10^{-7}$ T.

According to equation (16), the frequency shift of the eigenvalue at EP3 is

$$\Delta_\omega = g_{\text{EP3}}^{2/3} \Delta_B^{1/3} = \left(2\gamma/\sqrt{3}\right)^{2/3} \times (2\pi \times 0.025)^{1/3} \approx 2\pi \times 0.67 \text{ (MHz)}, \quad (28)$$

where $\gamma/2\pi \approx 3$ MHz is the measured damping rates of the two nearly identical YIG spheres.

In our experiment, the minimum value of the total output spectrum changes 21.5 dB around the EP3 when, e.g., $\Delta_B/2\pi = 0.025$ MHz, as illustrated in figure 3(e). The synthetic sensitivity factor is $G_{\text{syn}} = 21.5/0.025 = 860$. Correspondingly, the CPA-related sensitivity factor and the sensitivity factor at the EP3 are $G_{\text{CPA}} = 32.1$ and $G_{\text{EP3}} = 26.8$, respectively. Indeed, as shown in figure 4(b), the synthetic sensitivity factor is much larger than the respective sensitivity factors. Note that the smallest spectrum change that can be resolved by the vector network analyzer used in our experiment (KEYSIGHT PNA-L Network Analyzer N5232B) is $\delta A \sim 1 \times 10^{-13}$ dB. From the definition of the synthetic sensitivity factor, it follows that the detectable minimum change of the magnetic field δB_{min} is determined by

$$G_{\text{syn}} = 2\pi \frac{\delta A}{\gamma_e \delta B_{\text{min}}}. \quad (29)$$

Thus, we have

$$\delta B_{\text{min}} = \frac{2\pi \times 10^{-13}}{(2\pi \times 28 \times 10^3) \times 860} \approx 4.2 \times 10^{-21} \text{ (T)}, \quad (30)$$

which indicates that the detectable minimum change of the magnetic-field can reach the magnitude $\sim 10^{-21}$ T.

4. Conclusions

In summary, we have demonstrated a synthetically enhanced magnetic sensor using both CPA and EP3 in a pseudo-Hermitian cavity magnonic system. The sensitivity

enhancements associated with these two mechanisms are superimposed in a product manner, yielding a greatly amplified synthetic sensitivity. This synthetically enhanced sensitivity offers a new way to explore promising applications of precision metrology via hybrid non-Hermitian quantum systems.

Acknowledgments

This work is supported by the National Key Research and Development Program of China (No. 2022YFA1405200), National Natural Science Foundation of China (No. 92265202, No. 11934010, and No. 12174329), and the Fundamental Research Funds for the Central Universities (No. 2021FZZX001-02).

Appendix A. Dissipation rates of the cavity ports

The dissipation rates of the cavity ports are tuned by changing the lengths of antenna pins inserted into the cavity. The shorter the antenna pin is inserted into the cavity, the smaller the dissipation rate of the corresponding port is.

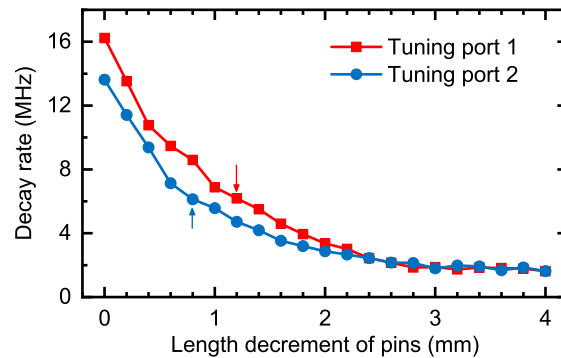


Figure A1. Precise adjustments of the dissipation rates of the two ports, i.e., κ_1 and κ_2 , by tuning the length decrements of the antenna pins. The shorter the pins are inside the cavity, the dissipation rates will be smaller. When the length decrements are larger than 3 mm, the dissipation rates of the two ports become nearly unchanged. This corresponds to the intrinsic dissipation rate κ_{int} of the cavity. The length decrements of the two pins used in our experiment are marked by the red and blue arrows.

In figure A1, we gradually reduce the length of the antenna pin inserted into the cavity, and finally the cavity loss converges to a finite value that corresponds to the intrinsic dissipation rate of the cavity, which is about 2 MHz in our experiment. Besides, the dissipation rates of the two ports satisfy $(\kappa_1 + \kappa_{\text{int}})/2\pi = 6$ MHz and $(\kappa_2 + \kappa_{\text{int}})/2\pi = 6$ MHz, as is illustrated with arrows in figure A1.

Appendix B. Non-Hermitian Hamiltonian of the system in the presence of coherent perfect absorption

In the rotating frame associated with the cavity frequency ω_c , the Hamiltonian can be written as

$$H_s/\hbar = \Delta_1 b_1^\dagger b_1 + \Delta_2 b_2^\dagger b_2 + g_1 \left(a^\dagger b_1 + a b_1^\dagger \right) + g_2 \left(a^\dagger b_2 + a b_2^\dagger \right), \quad (\text{B.1})$$

where $\Delta_{1(2)} = \omega_{1(2)} - \omega_c$ is the frequency detuning between the Kittel mode in the YIG sphere 1(2) and the cavity mode. The Langevin equations of the coupled system can now be written as

$$\begin{aligned} \dot{a} &= -\frac{i}{\hbar} [a, H_s] - (\kappa_1 + \kappa_2 + \kappa_{\text{int}}) a + \sqrt{2\kappa_1} a_1^{(\text{in})} + \sqrt{2\kappa_2} a_2^{(\text{in})}, \\ \dot{b}_1 &= -\frac{i}{\hbar} [b_1, H_s] - \gamma_1 b_1, \\ \dot{b}_2 &= -\frac{i}{\hbar} [b_2, H_s] - \gamma_2 b_2, \end{aligned} \quad (\text{B.2})$$

where κ_1 , κ_2 and κ_{int} are the dissipation rates of the cavity mode associated with port 1, port 2 and the intrinsic loss of the cavity, respectively, while γ_1 and γ_2 are the dissipation rates of the Kittel modes in the two YIG spheres. The input and output fields of the i th port, $a_i^{(\text{in})}$ and $a_i^{(\text{out})}$, obey the input-output relation

$$a_i^{(\text{in})} + a_i^{(\text{out})} = \sqrt{2\kappa_i} a, \quad i = 1, 2. \quad (\text{B.3})$$

When the coherent perfect absorption (CPA) occurs, $a_1^{(\text{out})} = a_2^{(\text{out})} = 0$, so

$$a_1^{(\text{in})} = \sqrt{2\kappa_1} a, \quad a_2^{(\text{in})} = \sqrt{2\kappa_2} a. \quad (\text{B.4})$$

The quantum Langevin equations in equation (B.2) become

$$\begin{aligned} \dot{a} &= -\frac{i}{\hbar} [a, H_s] + (\kappa_1 + \kappa_2 - \kappa_{\text{int}}) a, \\ \dot{b}_1 &= -\frac{i}{\hbar} [b_1, H_s] - \gamma_1 b_1, \\ \dot{b}_2 &= -\frac{i}{\hbar} [b_2, H_s] - \gamma_2 b_2, \end{aligned} \quad (\text{B.5})$$

which can be rewritten as

$$\begin{aligned} \dot{a} &= -\frac{i}{\hbar} [a, H_{\text{eff}}], \\ \dot{b}_1 &= -\frac{i}{\hbar} [b_1, H_{\text{eff}}], \\ \dot{b}_2 &= -\frac{i}{\hbar} [b_2, H_{\text{eff}}], \end{aligned} \quad (\text{B.6})$$

where

$$H_{\text{eff}}/\hbar = i\kappa_c a_1^\dagger a_1 + (\Delta_1 - i\gamma_1) b_1^\dagger b_1 + (\Delta_2 - i\gamma_2) b_2^\dagger b_2 + g_1 \left(a^\dagger b_1 + a b_1^\dagger \right) + g_2 \left(a^\dagger b_2 + a b_2^\dagger \right), \quad (\text{B.7})$$

with $\kappa_c \equiv \kappa_1 + \kappa_2 - \kappa_{\text{int}}$. When $\kappa_c > 0$, the CPA provides an effective gain to the cavity. In the matrix form, this non-Hermitian Hamiltonian can be written as

$$H_{\text{eff}}/\hbar = \begin{pmatrix} i\kappa_c & g_1 & g_2 \\ g_1 & \Delta_1 - i\gamma_1 & 0 \\ g_2 & 0 & \Delta_2 - i\gamma_2 \end{pmatrix}, \quad (\text{B.8})$$

Appendix C. Formulism of the output spectrum

The quantum Langevin equations of the cavity magnonic system have been illustrated in equation (B.2). It notes that when applying the Fourier transformations

$$x(t) = \frac{1}{\sqrt{2\pi}} \int_{-\infty}^{+\infty} x(\omega) e^{-i\omega t} d\omega, \quad x = a, b_1, b_2, \quad (\text{C.1})$$

we obtain the Langevin equations in the frequency domain,

$$\begin{aligned} -i\omega a(\omega) &= -\frac{i}{\hbar} [a(\omega), H_s(\omega)] - (\kappa_1 + \kappa_2 + \kappa_{\text{int}}) a(\omega) \\ &+ \sqrt{2\kappa_1} a_1^{(\text{in})}(\omega) + \sqrt{2\kappa_2} a_2^{(\text{in})}(\omega), \\ -i\omega b_j(\omega) &= -\frac{i}{\hbar} [b_j(\omega), H_s(\omega)] - \gamma_j b_j(\omega), \quad j = 1, 2. \end{aligned} \quad (\text{C.2})$$

Using the input-output relation

$$a_j^{(\text{in})}(\omega) + a_j^{(\text{out})}(\omega) = \sqrt{2\kappa_j} a(\omega), \quad j = 1, 2, \quad (\text{C.3})$$

we can obtain the general relations between the output fields, i.e., $a_1^{(\text{out})}$ and $a_2^{(\text{out})}$, and the input fields, i.e., $a_1^{(\text{in})}$ and $a_2^{(\text{in})}$:

$$\begin{aligned} a_1^{(\text{out})} &= r_{11} a_1^{(\text{in})} + t_{12} a_2^{(\text{in})}, \\ a_2^{(\text{out})} &= r_{22} a_2^{(\text{in})} + t_{21} a_1^{(\text{in})}, \end{aligned} \quad (\text{C.4})$$

with the transmission and reflection coefficients

$$\begin{aligned} t_{12}(\omega) &= t_{21}(\omega) = -\frac{2\sqrt{\kappa_1\kappa_2}}{m + in}, \\ r_{jj}(\omega) &= -1 - \frac{2\kappa_j}{m + in}, \quad j = 1, 2, \end{aligned} \quad (\text{C.5})$$

where

$$\begin{aligned} m &= -(\kappa_1 + \kappa_2 + \kappa_{\text{int}}) - \sum_{j=1}^2 \frac{g_j^2 \gamma_j}{(\omega - \omega_j)^2 + \gamma_j^2}, \\ n &= (\omega - \omega_c) - \sum_{j=1}^2 \frac{g_j^2 (\omega - \omega_j)}{(\omega - \omega_j)^2 + \gamma_j^2}. \end{aligned} \quad (\text{C.6})$$

Note that the output field of each port is the sum of the reflection signal at that port and the transmission signal from the other port. The amplitudes of the output fields at the two ports of the cavity are

$$\begin{aligned} S_1(\omega) &= r_{11}(\omega)\sqrt{p}e^{-i\phi} + t_{12}(\omega), \\ S_2(\omega) &= r_{22}(\omega) + t_{21}(\omega)\sqrt{p}e^{-i\phi}, \end{aligned} \quad (\text{C.7})$$

where p and ϕ denote, respectively, the power ratio and phase difference between the two input fields.

The total output spectrum is obtained by summing the output-field intensities at the two ports:

$$\begin{aligned} |S_{\text{tot}}(\omega)|^2 &\equiv |S_1(\omega)|^2 + |S_2(\omega)|^2 \\ &= \frac{(p+1) \left| [m(\omega) + 2\sqrt{\kappa_1\kappa_2}e^{i\phi}/\sqrt{p} + 2\kappa_1] + in(\omega) \right|^2}{m(\omega)^2 + n(\omega)^2} \\ &\quad + \frac{\left(\sqrt{p}e^{-i\phi} - \sqrt{\kappa_1/\kappa_2} \right) k(\omega)}{m(\omega)^2 + n(\omega)^2}, \end{aligned} \quad (\text{C.8})$$

where

$$\begin{aligned} k(\omega) &= 4 \left(\sqrt{\kappa_1\kappa_2} + \kappa_2 e^{i\phi}/\sqrt{p} \right)^2 \left(\sqrt{p}e^{-i\phi} - \sqrt{\kappa_1/\kappa_2} \right) \\ &\quad + 4 \left(\sqrt{\kappa_1\kappa_2} + \kappa_2 e^{i\phi}/\sqrt{p} \right) \left(m + 2\sqrt{\kappa_1\kappa_2}e^{i\phi}/\sqrt{p} + 2\kappa_1 \right). \end{aligned} \quad (\text{C.9})$$

References

- [1] Bender C M 2007 Making sense of non-Hermitian Hamiltonians *Rep. Prog. Phys.* 70 947
- [2] Rotter I 2009 A non-Hermitian Hamilton operator and the physics of open quantum systems *J. Phys. A: Math. Theor.* 42 153001
- [3] Shen H, Zhen B and Fu L 2018 Topological Band Theory for Non-Hermitian Hamiltonians *Phys. Rev. Lett.* 120 146402
- [4] Leykam D, Bliokh K Y, Huang C, Chong Y D and Nori F 2017 Edge Modes, Degeneracies, and Topological Numbers in Non-Hermitian Systems *Phys. Rev. Lett.* 118 040401
- [5] Bergholtz E J, Budich J C and Kunst F K 2021 Exceptional topology of non-Hermitian systems *Rev. Mod. Phys.* 93 015005
- [6] Heiss W D 2004 Exceptional points of non-Hermitian operators *J. Phys. A: Math. Gen.* 37 2455
- [7] Heiss W D 2012 The physics of exceptional points *J. Phys. A: Math. Theor.* 45 444016
- [8] Rüter C E, Makris K G, El-Ganainy R, Christodoulides D N, Segev M and Kip D 2010 Observation of parity-time symmetry in optics *Nat. Phys.* 6 192-195
- [9] Chang L, Jiang X, Hua S, Yang C, Wen J, Jiang L, Li G, Wang G and Xiao M 2014 Parity-time symmetry and variable optical isolation in active-passive-coupled microresonators *Nat. Photonics* 8 524-529
- [10] Peng B, Özdemir S K, Lei F, Monifi F, Gianfreda M, Long G L, Fan S, Nori F, Bender C M and Yang L 2014 Parity-time-symmetric whispering-gallery microcavities *Nat. Phys.* 10 394-398
- [11] Makris K G, El-Ganainy R, Christodoulides D N and Musslimani Z H 2008 Beam Dynamics in \mathcal{PT} Symmetric Optical Lattices *Phys. Rev. Lett.* 100 103904

- [12] Zhen B, Hsu C W, Igarashi Y, Lu L, Kaminer I, Pick A, Chua S-L, Joannopoulos J D and Soljačić M 2015 Spawning rings of exceptional points out of Dirac cones *Nature* 525 354-358
- [13] Guo A, Salamo G J, Duchesne D, Morandotti R, Volatier-Ravat M, Aimez V, Siviloglou G A and Christodoulides D N 2009 Observation of \mathcal{PT} -Symmetry Breaking in Complex Optical Potentials *Phys. Rev. Lett.* 103 093902
- [14] Doppler J, Mailybaev A A, Böhm J, Kuhl U, Girschik A, Libisch F, Milburn T J, Rabl P, Moiseyev N and Rotter S 2016 Dynamically encircling an exceptional point for asymmetric mode switching *Nature* 537 76-79
- [15] Brandstetter M, Liertzer M, Deutsch C, Klang P, Schöberl J, Türeci H E, Strasser G, Unterrainer K and Rotter S 2014 Reversing the pump dependence of a laser at an exceptional point *Nat. Commun.* 5 4034
- [16] Lin Z, Pick A, Lončar M and Rodriguez A W 2016 Enhanced Spontaneous Emission at Third-Order Dirac Exceptional Points in Inverse-Designed Photonic Crystals *Phys. Rev. Lett.* 117 107402
- [17] Feng L, Wong Z J, Ma R M, Wang Y and Zhang X 2014 Single-mode laser by parity-time symmetry breaking *Science* 346 972-975
- [18] Hodaei H, Miri M A, Heinrich M, Christodoulides D N and Khajavikhan M 2014 Parity-time-symmetric microring lasers *Science* 346 975-978
- [19] Dembowski C, Gräf H D, Harney H L, Heine A, Heiss W D, Rehfeld H and Richter A 2001 Experimental Observation of the Topological Structure of Exceptional Points *Phys. Rev. Lett.* 86 787
- [20] Xu Y, Wang S-T and Duan L-M 2017 Weyl Exceptional Rings in a Three-Dimensional Dissipative Cold Atomic Gas *Phys. Rev. Lett.* 118 045701
- [21] Zhou H, Peng C, Yoon Y, Hsu C W, Nelson K A, Fu L, Joannopoulos J D, Soljačić M and Zhen B 2018 Observation of bulk Fermi arc and polarization half charge from paired exceptional points *Science* 359 1009-1012
- [22] Xu H, Mason D, Jiang L and Harris J G E 2016 Topological energy transfer in an optomechanical system with exceptional points *Nature* 537 80-83
- [23] Hassan A U, Zhen B, Soljačić M, Khajavikhan M and Christodoulides D N 2017 Dynamically Encircling Exceptional Points: Exact Evolution and Polarization State Conversion *Phys. Rev. Lett.* 118 093002
- [24] Özdemir Ş K, Rotter S, Nori F and Yang L 2019 Parity-time symmetry and exceptional points in photonics *Nat. Mater.* 18 783-798
- [25] Miri M A and Alù A 2019 Exceptional points in optics and photonics *Science* 363 eaar7709
- [26] Parto M, Liu Y G N, Bahari B, Khajavikhan M and Christodoulides D N 2020 Non-Hermitian and topological photonics: optics at an exceptional point *Nanophotonics* 10 403-423
- [27] Zhang D, Luo X-Q, Wang Y-P, Li T-F and You J Q 2017 Observation of the exceptional point in cavity magnon-polaritons, *Nat. Commun.* 8 1368
- [28] Liu H, Sun D, Zhang C, Groesbeck M, Mclaughlin R and Vardeny Z V 2019 Observation of exceptional points in magnonic parity-time symmetry devices *Sci. Adv.* 5 eaax9144
- [29] Ding K, Ma G, Xiao M, Zhang Z Q and Chan C T 2016 Emergence, Coalescence, and Topological Properties of Multiple Exceptional Points and Their Experimental Realization *Phys. Rev. X* 6 021007
- [30] Jing H, Özdemir S K, Lü X-Y, Zhang J, Yang L and Nori F 2014 \mathcal{PT} -symmetric phonon laser *Phys. Rev. Lett.* 113 053604
- [31] Lü X-Y, Jing H, Ma J-Y and Wu Y 2015 \mathcal{PT} -symmetry-breaking chaos in optomechanics *Phys. Rev. Lett.* 114 253601
- [32] Wiersig J 2014 Enhancing the Sensitivity of Frequency and Energy Splitting Detection by Using Exceptional Points: Application to Microcavity Sensors for Single-Particle Detection *Phys. Rev. Lett.* 112 203901
- [33] Hodaei H, Hassan A U, Wittek S, Garcia-Gracia H, El-Ganainy R, Christodoulides D N and Khajavikhan M 2017 Enhanced sensitivity at higher-order exceptional points *Nature* 548 187-

191

- [34] Chen W, Özdemir Ş K, Zhao G, Wiersig J and Yang L 2017 Exceptional points enhance sensing in an optical microcavity *Nature* 548 192-196
- [35] Zhong Q, Ren J, Khajavikhan M, Christodoulides D N, Özdemir Ş K and El-Ganainy R 2019 Sensing with Exceptional Surfaces in Order to Combine Sensitivity with Robustness *Phys. Rev. Lett.* 122 153902
- [36] Lai Y-H, Lu Y-K, Suh M-G, Yuan Z and Vahala K 2019 Observation of the exceptional-point-enhanced Sagnac effect *Nature* 576 65-69
- [37] Wiersig J 2020 Review of exceptional point-based sensors *Photonics Research* 8 1457-1467
- [38] Tang W, Jiang X, Ding K, Xiao Y-X, Zhang Z-Q, Chan C T and Ma G 2020 Exceptional nexus with a hybrid topological invariant *Science* 370 1077-1080
- [39] Budich J C and Bergholtz E J 2020 Non-Hermitian Topological Sensors *Phys. Rev. Lett.* 125 180403
- [40] Mostafazadeh A 2002 Pseudo-Hermiticity versus PT symmetry: The necessary condition for the reality of the spectrum of a non-Hermitian Hamiltonian *J. Math. Phys.* 43 205-214
- [41] Mostafazadeh A 2002 Pseudo-Hermiticity versus PT-symmetry. II. A complete characterization of non-Hermitian Hamiltonians with a real spectrum *J. Math. Phys.* 43 2814-2816
- [42] Wang Z-Q, Wang Y-P, Yao J, Shen R-C, Wu W-J, Qian J, Li J, Zhu S-Y and You J Q 2022 Giant spin ensembles in waveguide magnonics *Nat. Commun.* 13 7580
- [43] Chong Y D, Ge L, Cao H and Stone A D 2010 Coherent Perfect Absorbers: Time-Reversed Lasers *Phys. Rev. Lett.* 105 053901
- [44] Chong Y D, Ge L and Stone A D 2011 \mathcal{PT} -Symmetry Breaking and Laser-Absorber Modes in Optical Scattering Systems *Phys. Rev. Lett.* 106 093902
- [45] Sun Y, Tan W, Li H-Q, Li J and Chen H 2014 Experimental Demonstration of a Coherent Perfect Absorber with PT Phase Transition *Phys. Rev. Lett.* 112 143903
- [46] Baranov D G, Krasnok A, Shegai T, Alù A and Chong Y 2017 Coherent perfect absorbers: Linear control of light with light *Nat. Rev. Mater.* 2 17064
- [47] Soleymani S, Zhong Q, Mokim M, Rotter S, El-Ganainy R and Özdemir Ş K 2022 Chiral and degenerate perfect absorption on exceptional surfaces, *Nat. Commun.* 13 599
- [48] Zhang G-Q, Wang Y and Xiong W 2023 Detection sensitivity enhancement of magnon Kerr nonlinearity in cavity magnonics induced by coherent perfect absorption *Phys. Rev. B* 107 064417
- [49] Kawabata K, Shiozaki K, Ueda M and Sato M 2019 Symmetry and Topology in Non-Hermitian Physics, *Phys. Rev. X* 9 041015
- [50] Rivero J D H and Ge L 2020 Pseudochirality: A Manifestation of Noether's Theorem in Non-Hermitian Systems *Phys. Rev. Lett.* 125 083902
- [51] Zhang G-Q and You J Q 2019 Higher-order exceptional point in a cavity magnonics system *Phys. Rev. B* 99 054404